Relative Orbit Estimation with Wide Field of View Binary X-ray Sensing

Andrea López
University of Colorado Boulder
Julian Hammerl, and Hanspeter Schaub
University of Colorado Boulder

ABSTRACT

On-orbit, passive detection of objects in the vicinity of a spacecraft is a desirable capability for Space Situational Awareness applications, especially in orbit regions that are not illuminated by the Sun. The detection method proposed consists of exploiting the ambient plasma-induced x-ray emission to detect a target object using a cluster of simple, off-the-shelf x-ray spectrometers mounted on a rotating platform. Earlier work studied the application of this approach to targets that are in a static relative location to the sensor. This work explores J_2 perturbed orbits for relative orbit determination, leveraging the nonlinearities in the models to improve the observability of the system. Acquisition/loss of signal events are used in conjunction with a dynamic model of the target motion to obtain the target heading and relative motion by employing a sequential filtering approach. The study explores the impact of the trigger sampling frequency and the sensor platform rotation rate on the nonlinear relative motion estimation performance.

1. INTRODUCTION

Space Situational Awareness (SSA) is a topic widely researched in the near-Earth region, involving the detection and tracking of objects orbiting the Earth without direct interaction with these objects. At present only a handful of spacecraft are in the cislunar region further than GEO, but the presence of vehicles in the lunar vicinity is anticipated to increase in the upcoming years, with robotic exploration missions, satellite communication and navigation systems, or the Gateway [5, 8]. With the increased presence on spacecraft in this region, on-orbit cislunar SSA capabilities will become an asset in the near future, not only for debris tracking purposes but also for proximity operation applications with non-cooperative spacecraft [3, 10].

A new method of using ambient plasma-induced x-rays to detect objects in the neighborhood of a spacecraft is proposed for GEO and the cislunar region. Energetic electrons ($>$ few 100 eV) present in the ambient plasma [6, 15] interact with atomic nuclei exciting the release of characteristic x-rays and bremsstrahlung x-rays [19]. This project investigates the use of wide FOV x-ray detector in the form of a cluster of commercial

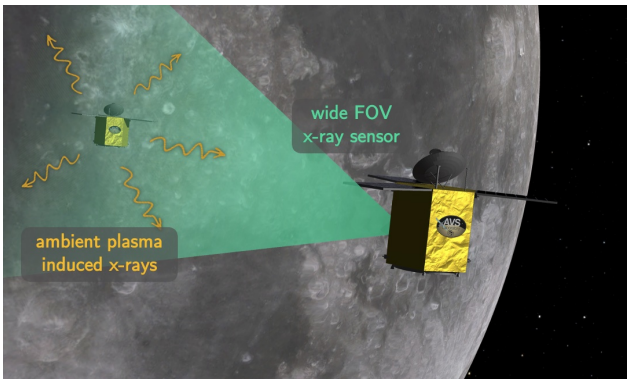

Fig. 1: Illustration of wide FOV sensor concept detecting a nearby spacecraft

off-the-shelf x-ray sensors to detect objects in the vicinity of a spacecraft, exploiting the natural interactions taking place in the ambient plasma.

The sensors considered in this research are Si-PIN photodiode x-ray spectrometers[1], and the signal is modeled as an on/off signal. A measurement is therefore obtained when the signal changes from on to off (or viceversa) on a particular sensor, knowing that this event takes place when the target object is at the edge of the field of view of that sensor. Thus, at the time of the change-of-signal event (or *trigger* event), the angle between the pointing of the sensor (known) and the target heading is the field of view cone half angle. To increment the number of such events, the cluster of sensors is mounted on a platform that is rotating at a known constant angular rate relative to the spacecraft body. This methodology provides an angles-only approach to the initial relative motion estimation problem, as range measurements are not available. Prior work explores a variety of sensor configurations for one or multiple sensor clusters, analyzing the performance for obtaining a heading for a static target (i.e., not moving with respect to the observer spacecraft) [11]. For a dynamic target, linear relative motion examples (e.g., unforced double integrator dynamics) introduce dynamical observability challenges [12]. This work explores more realistic models for the relative orbit dynamics that could be encountered in an on-orbit scenario. The linearized relative orbital motion in unobservable with angles-only measurements [20], but recent approaches to ROD exploit the nonlinearities in the filter dynamics and measurement equations to improve the observability of the problem using vision-based sensors [9, 13, 4].

A method for using a batch of trigger events to obtain estimated headings, which are then the input for a sequential filter, was introduced in previous work [12]. A variation of this approach is used here, in which the trigger events after a full revolution of the platform are combined to estimate the target bearing angles at an intermediate time instant. This work follows the approach developed by Sullivan et al. [17] to sequentially estimate the relative orbit of a target object using the Unscented Kalman Filter proposed by Julier et al. [7]. This nonlinear variant of the Kalman Filter is used to to leverage the nonlinearities in the dynamics and measurement model that contain range information. The filter takes in synchronous bearing angles measurements and estimates mean relative orbit elements (ROE) in a scenario subject to J_2 perturbation effects.

First, a description of the sensor configuration and the test cases used in this work is given. A proposed approach is then introduced to obtain estimated headings of a target from the on/off trigger events, and the effects of a dynamic target, sampling frequency and rotation speed of the platform are discussed. The relative position estimation description, dynamic model, and measurement model are presented. Finally, the results obtained with the present estimation approach are discussed, and future work directions are considered.

2. PROBLEM STATEMENT

The sensor configuration used for this work consists of a cluster of six x-ray sensors, each of them with a field of view of 15° (half-cone). The sensors are mounted on a rotating platform with increasing elevation angles of $\phi = 0°$, 15°, 30°, 45°, 60°, and 75°, respectively, as shown in Fig. 2a. The platform reference frame is denoted $\mathcal{P} : \{\hat{\boldsymbol{p}}_1, \hat{\boldsymbol{p}}_2, \hat{\boldsymbol{p}}_3\}$. The sensors rotate about the platform's $\hat{\boldsymbol{p}}_3$ axis with prescribed angular velocity $\boldsymbol{\omega} = \omega\hat{\boldsymbol{p}}_3$ where $\hat{\boldsymbol{p}}_3$ is a body-fixed axis. For the sake of simplicity, it is assumed here that the servicer attitude is aligned at all times with the Hill frame $\mathcal{O} : \{\hat{\boldsymbol{o}}_r, \hat{\boldsymbol{o}}_\theta, \hat{\boldsymbol{o}}_h\}$, where $\hat{\boldsymbol{o}}_r$ is in the orbit radial direction, $\hat{\boldsymbol{o}}_h$ is parallel to the orbit momentum vector and $\hat{\boldsymbol{o}}_\theta$ completes the right-handed coordinate system. An intermediate reference frame fixed to the servicer spacecraft is defined as $\mathcal{I} : \{\hat{\boldsymbol{i}}_1, \hat{\boldsymbol{i}}_2, \hat{\boldsymbol{i}}_3\}$, where $\hat{\boldsymbol{i}}_1 = \hat{\boldsymbol{o}}_r$, $\hat{\boldsymbol{i}}_2 = \hat{\boldsymbol{o}}_h$ and $\hat{\boldsymbol{i}}_3 = -\hat{\boldsymbol{o}}_\theta$, such that, for a target spacecraft behind the servicer spacecraft, the along-track separation is mainly contained in the $\hat{\boldsymbol{i}}_3$ direction. The platform is mounted on the spacecraft tilted 45° about $\hat{\boldsymbol{i}}_1 = \hat{\boldsymbol{o}}_r$ with respect to the intermediate and Hill frames. The direct cosine matrices (DCMs) to map vectors from the orbit frame $\mathcal{O}$ into the intermediate frame $\mathcal{I}$ $[IO]$, and from the intermediate frame $\mathcal{I}$ into the platform frame $\mathcal{P}$ $[PI]$ are, respectively:

$$[IO] = \begin{bmatrix} 1 & 0 & 0 \\ 0 & 0 & 1 \\ 0 & -1 & 0 \end{bmatrix} \tag{1}$$

[1] https://www.amptek.com/internal-products/x-123-complete-x-ray-spectrometer-with-si-pin-detector

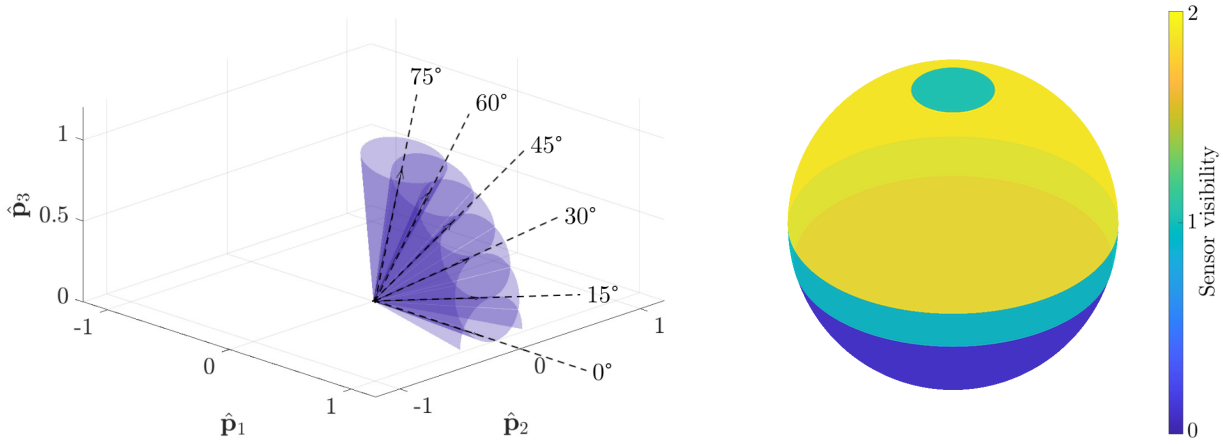

(a) (b)

Fig. 2: Illustration of sensor configuration with sensor elevation angles (a) and visibility map around the servicer (b) for the sensor cluster concept used [12]

$$[PI] = \begin{bmatrix} 1 & 0 & 0 \\ 0 & \cos\gamma & -\sin\gamma \\ 0 & \sin\gamma & \cos\gamma \end{bmatrix} \tag{2}$$

where $\gamma = 45°$ is the tilt of the platform.

More details on how the configuration of the sensors, positioning of the platform and platform motion affect the availability and effectiveness of measurements can be found in [11].

The performance of the proposed approach is tested for two relative orbit cases. The chief is orbiting the earth whose gravity field includes the J_2 perturbation. The mean absolute orbit elements of the chief at the initial time used for the analysis are:

$$\boldsymbol{x}_{\boldsymbol{oe},c} = (a = 32434 \text{ km}, e = 0.3, i = 10°, \Omega = 120°, \omega = 10°, M = 180°)^T \tag{3}$$

Here a is the semi-major axis, e is the eccentricity, i is the inclination angle, Ω is the ascending node, ω is the argument of periapses and M is the mean anomaly angle. This describes an arbitrary eccentric orbit with apogee at GEO radius and perigee at about 22700 km. The initial mean orbit element differences for the two relative orbit cases (where $\Delta(\cdot) = (\cdot)_d - (\cdot)_c$) are provided in Table 1. Case 1 is a relative orbit with in-plane and out-of-plane oscillations and mean along-track separation between 20 km and 60 km initially. The difference in semi-major axis results in the along-track separation being reduced in consecutive orbits. Case 2 describes a simple lead-follower configuration with mean along-track separation of about 100 km.

Table 1: Relative orbit cases description in classic element differences

	Δa [km]	Δe	Δi [rad]	$\Delta\omega$ [rad]	$\Delta\Omega$ [rad]	ΔM_0 [rad]
Case 1	-1.5e-1	5e-5	5e-4	1.5e-4	1.5e-4	-1.5e-3
Case 2	0	0	0	0	0	-3e-3

3. HEADING ESTIMATION OF A DYNAMIC TARGET

The relative position vector of the target spacecraft with respect to the servicer is $\delta\boldsymbol{r} = \boldsymbol{r}_d - \boldsymbol{r}$, where $\boldsymbol{r}_d$ is the position of the target (deputy) spacecraft and $\boldsymbol{r}$ is the position of the servicer (chief) spacecraft. The heading vector is defined as $\boldsymbol{h} = \delta\boldsymbol{r}/\|\delta\boldsymbol{r}\|$. The bearing angles that constitute a measurement are azimuth θ

and elevation ε about the platform boresight, calculated as

$$y = \begin{pmatrix} \theta \\ \varepsilon \end{pmatrix} = \begin{pmatrix} \arctan({}^{\mathcal{P}}h_2/{}^{\mathcal{P}}h_1) \\ \arcsin({}^{\mathcal{P}}h_3) \end{pmatrix} \tag{4}$$

When a trigger event is recorded, the target is at the edge of the field of view of sensor i:

$$\boldsymbol{m}_i^T \boldsymbol{h} = \cos f \tag{5}$$

where $\boldsymbol{m}_i$ is the pointing vector of sensor i and f is the half-angle of the field of view cone of the sensors. For a static case with constant heading, in order to obtain said heading, multiple trigger events are combined into matrix form:

$$\begin{bmatrix} \boldsymbol{m}_1^T \\ \boldsymbol{m}_2^T \\ ... \\ \boldsymbol{m}_p^T \end{bmatrix} \boldsymbol{h} = \begin{bmatrix} \cos f \\ \cos f \\ ... \\ \cos f \end{bmatrix} \tag{6}$$

where $\boldsymbol{m}_j$ is the pointing vector of the sensor giving the j^{th} trigger event and p the total number of trigger events considered. This equation is then in the classic matrix-vector form $M\boldsymbol{a} = \boldsymbol{b}$, with solution $\bar{\boldsymbol{a}} = M^+\boldsymbol{b}$, with M^+ being the Moore-Penrose inverse of matrix M ($\bar{(\cdot)}$ will explicitly indicate estimated quantity). In cases where rank$(M) \geq 3$, $\bar{\boldsymbol{a}}$ is the least-squares solution for this problem. However, if rank$(M) < 3$ (i.e., if there are less than two unique trigger events to be considered), the problem is under-determined and the Moore-Penrose inverse provides the minimum norm solution.

Reference [11] assumes the heading to remain constant during the collection of the trigger events. With the described sensor configuration, after one full revolution the instrument coverage is 2.52π sr, with a 1.93π sr being covered by at least two sensors (see Fig. 2b). The subsequent analysis revealed that, for headings within the field of view of two sensors during the revolution, four unique trigger events are obtained: an "on" trigger and an "off" trigger from each of the two sensors. For this case, the exact heading can be obtained, down to the accuracy of the knowledge of the pointing of the sensors. If the target is within the field of view of only one of the sensors after a revolution, two trigger events are obtained, making the problem under-determined and infinitely many solutions exist. Using the unit vector constraint, two heading solutions remain. Thus, it is not possible in this case to unequivocally determine the target heading. Using instead the minimum norm solution, the maximum divergence between the estimated and true heading is $\cos^{-1}(\boldsymbol{h}^T\bar{\boldsymbol{h}}) = f$.

In the relative motion scenario in hand, the heading is not constant but varies slowly over a time scale of hours. A fixed time interval corresponding to a full revolution of the sensor platform is set as the time period to collect trigger events that are combined to obtain a heading. The rotational speeds considered are in the order of degrees per second, making the revolution time in the order of minutes. The knowledge of previous heading estimates can be leveraged in the under-determined case with two valid heading solutions, resolving the ambiguity by selecting the heading solution closest to the previous heading estimate (higher order finite difference conditions can also be implemented).

Equation 6 assumes the heading is unchanged for all trigger events and therefore the estimated heading obtained with this method introduces an error. With a rotational speed of the platform of, for example, one degree per second, the maximum time period between an on trigger and an off trigger for a static target is 30 seconds (the time needed for the sensor to move 30°, the full cone of the field of view). Within this time frame, the variation in target heading is very small and can be approximated as linear. The heading obtained is then the mean of the headings at the times of the trigger events, and the time assigned to the measurement is the mean of the trigger events times. In Fig. 3, a heading estimation result is shown for an angular speed of $\omega = 0.5$ deg/s. Another source of error affecting the heading estimation is associated with the sampling frequency f_s, the frequency at which the signal-no signal checks are performed. For high platform angular speeds and low sampling frequency, a non-negligible variation of the sensor pointing occurs between adjacent samples, resulting in a larger uncertainty in sensor positioning and timing at the instant of signal acquisition/loss. The accuracy of the heading estimation in a dynamic case is therefore highly dependent on both angular speed of the platform and sampling frequency. To quantify this effect, several

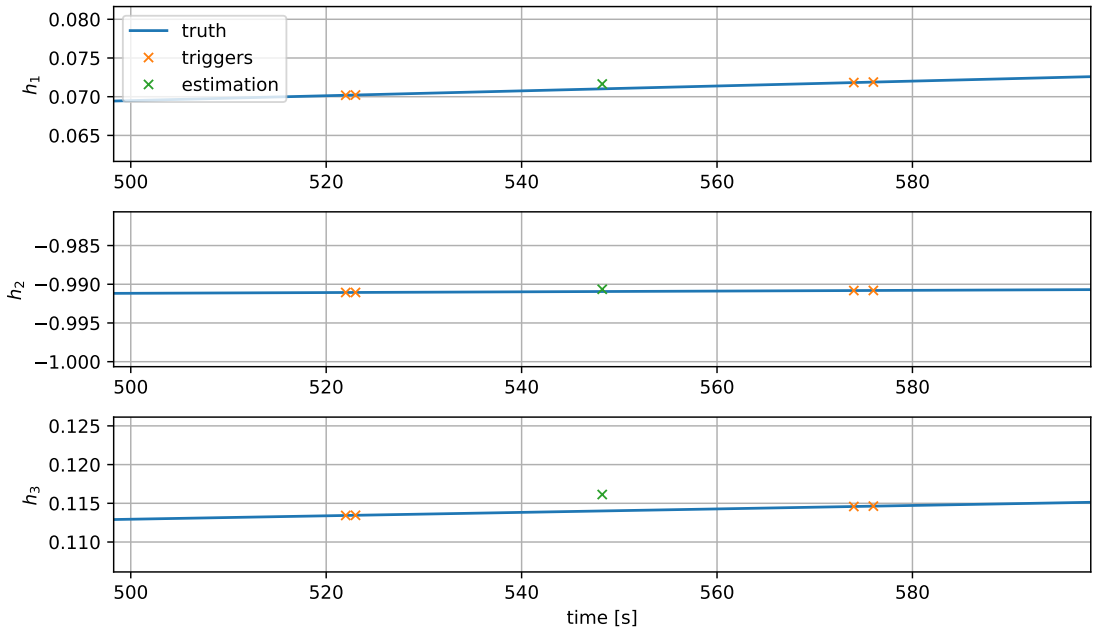

Fig. 3: Example of heading estimation. The blue line plots the true heading, the yellow crosses mark the times of trigger events and the green cross marks the estimated heading.

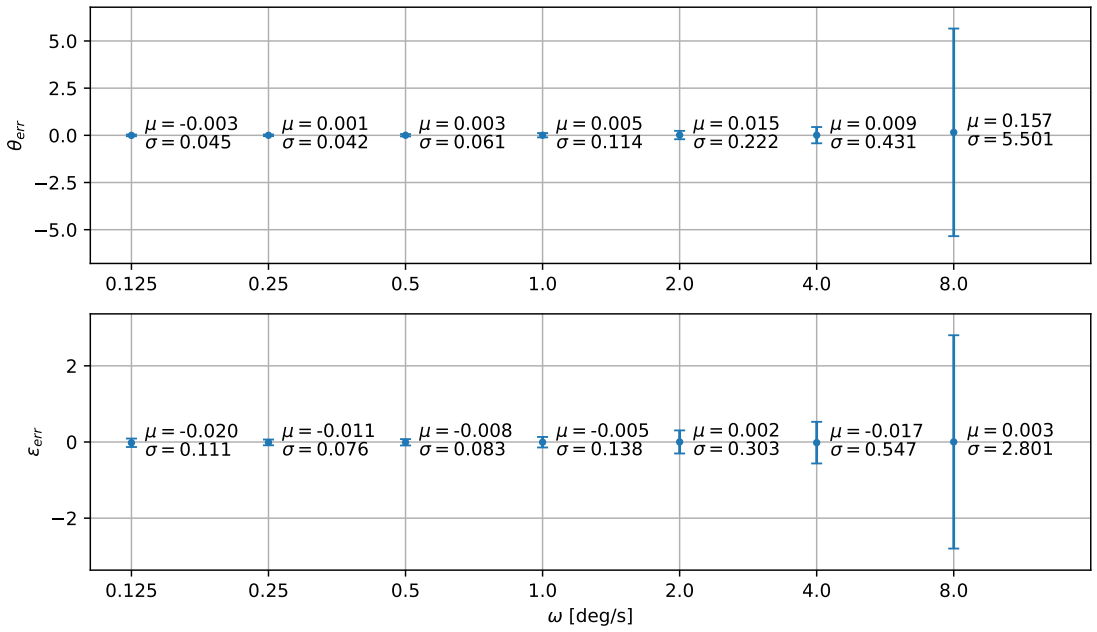

Fig. 4: Mean and standard deviation of the error in bearing angle estimation for case 1, for a sampling frequency of $f_s = 1$ Hz

values of $\omega \cdot f_s$ have been tested, calculating the mean and the root mean square of the error between the estimated heading and true heading at the measurement time. Figure 4 shows the error statistics in bearing angles for a sampling frequency of $f_s = 1$ Hz and platform angular speeds ranging from $\omega = 0.125$ deg/s to $\omega = 8$ deg/s for the relative orbit case 1. Table 2 collects this same information for the two relative orbit cases considered. A similar analysis was performed for different sampling frequencies yielding comparable result trends for $\omega = 0.5$ deg/s, and the error statistics are collected in Table 3.

Table 2: Error statistics with ω of the bearing angle estimations for the two relative orbit cases in degrees

			ω [deg/s]						
			0.125	0.25	0.5	1	2	4	8
Case 1	θ	μ	-0.006	-0.011	-0.007	-0.005	-0.001	0.030	0.363
		σ	0.061	0.064	0.073	0.126	0.227	0.489	7.574
	ε	μ	0.029	0.029	0.016	0.009	0.005	0.022	0.256
		σ	0.317	0.211	0.125	0.131	0.250	0.1563	3.479
Case 2	θ	μ	-0.001	-0.007	0.002	0.003	0.408	0.696	1.360
		σ	0.021	0.049	0.090	0.130	8.473	11.124	15.693
	ε	μ	0.001	0.003	0.004	0.058	0.195	0.332	0.762
		σ	0.376	0.236	0.124	1.768	3.056	3.765	5.944

Table 3: Error statistics with f_s of the bearing angle estimation for the two relative orbit cases in degrees

			f_s [Hz]		
			10	1	0.1
Case 1	θ	μ	0.001	0.001	0.063
		σ	0.014	0.079	0.803
	ε	μ	0.005	-0.006	0.072
		σ	0.103	0.135	0.841
Case 2	θ	μ	-0.001	-0.003	0.026
		σ	0.009	0.090	0.813
	ε	μ	-0.001	0.007	-0.070
		σ	0.048	0.156	1.395

For a given sampling frequency, slower rotations of the platform provide more accurate results. However, because only one estimated heading is obtained per full revolution, slower angular velocities lead to fewer, more dispersed measurements. For a given angular speed of the platform, higher sampling frequencies provide more accurate results. However, a higher sampling frequency translates to smaller photon collection times, which can lead to spurious or missed detections. For this work, a sampling frequency of $f_s = 1$ Hz and angular speed of $\omega = 0.5$ deg/s is adopted, resulting in a revolution time (an therefore, an approximate cadence of heading measurements) of 12 minutes.

4. RELATIVE POSITION ESTIMATION

The unscented Kalman filter (UKF) adopted here to estimate the relative state of the target uses nonlinear dynamics and measurement models. This filter uses a set of sigma points to approximate the distribution of the state. The UKF algorithm and unscented transform equations can be found in Appendix A.

4.1 Relative orbit element set

Many different representations exist for describing the relative motion of two objects in orbit. The absolute orbit of a satellite can be expressed in the classical Keplerian orbital elements $\boldsymbol{x_{oe}} = (a, e, i, \omega, \Omega, M)^T$. The

relative motion of a deputy spacecraft with respect to the chief can be parameterized using the dimensionless relative orbit description proposed by D'Amico [2] as:

$$\delta\boldsymbol{\alpha} = f(\boldsymbol{x}_{\boldsymbol{\alpha e},d}, a_c, i_c) - f(\boldsymbol{x}_{\boldsymbol{\alpha e},c}, a_c, i_c) \tag{7}$$

where

$$f(\boldsymbol{x}_{\boldsymbol{\alpha e}}, a_c, i_c) = \begin{pmatrix} a/a_c \\ u + \Omega\cos i_c \\ e\cos\omega \\ e\sin\omega \\ i \\ \Omega\sin i_c \end{pmatrix} \tag{8}$$

with $u = M + \omega$ the mean argument of latitude.

The resulting relative orbit description is:

$$\delta\boldsymbol{\alpha} = \begin{pmatrix} (a_d - a_c)/a_d \\ (u_d - u_c) + (\Omega_d - \Omega_c)\cos i_c \\ e_d\cos\omega_d - e_c\cos\omega_c \\ e_d\sin\omega_d - e_c\sin\omega_c \\ i_d - i_c \\ (\Omega_d - \Omega_c)\sin i_c \end{pmatrix} = \begin{pmatrix} \delta a \\ \delta\lambda \\ \delta e_x \\ \delta e_y \\ \delta i_x \\ \delta i_y \end{pmatrix} \tag{9}$$

The components of the relative state $\delta\boldsymbol{\alpha}$ are the relative non-dimensional semi-major axis δa, the relative mean longitude $\delta\lambda$, and the relative eccentricity and inclination vectors, $\delta\boldsymbol{e}$ and $\delta\boldsymbol{i}$. These relative vectors provide a description of the in-plane and out-of-plane relative motion oscillations, and can be expressed in polar notation as:

$$\delta\boldsymbol{e} = \begin{pmatrix} \delta e_x \\ \delta e_y \end{pmatrix} = \delta e \begin{pmatrix} \cos\varphi \\ \sin\varphi \end{pmatrix} \tag{10}$$

$$\delta\boldsymbol{i} = \begin{pmatrix} \delta i_x \\ \delta i_y \end{pmatrix} = \delta i \begin{pmatrix} \cos\theta \\ \sin\theta \end{pmatrix} \tag{11}$$

This relative element description based on relative eccentricity $\delta\boldsymbol{e}$ and relative inclination $\delta\boldsymbol{i}$ vectors are particularly useful in collision avoidance and passive safety scenarios to control the separation in the plane perpendicular to the chief's direction of motion. Using this set, the mean along-track separation between the two spacecraft, which is only weakly observable and thus associated with larger uncertainty, is contained in a single element $\delta\lambda$.

4.2 Dynamics model

The filter used in this estimation work is the Unscented Kalman Filter (UKF), which does not require a linearizarion of the equations of motion to propagate the state vector. Instead, it numerically propagates the state using the full equations of motion. With the selected relative orbital element set, the equations of motion are:

$$\delta\dot{\boldsymbol{\alpha}} = \dot{\boldsymbol{f}}(\boldsymbol{x}_{\boldsymbol{\alpha e},d}, a_c, i_c) - \dot{\boldsymbol{f}}(\boldsymbol{x}_{\boldsymbol{\alpha e},c}, a_c, i_c) \tag{12}$$

For a dynamics model that includes J_2 perturbations, the secular variations of the classical orbital elements are obtained from Lagrange's planetary equations:

$$\begin{cases} \dfrac{\mathrm{d}a}{\mathrm{d}t} = 0 & \text{(13a)} \\ \dfrac{\mathrm{d}e}{\mathrm{d}t} = 0 & \text{(13b)} \\ \dfrac{\mathrm{d}i}{\mathrm{d}t} = 0 & \text{(13c)} \\ \dfrac{\mathrm{d}\omega}{\mathrm{d}t} = \dfrac{3}{2}\gamma n(5\cos^2 i - 1) & \text{(13d)} \\ \dfrac{\mathrm{d}\Omega}{\mathrm{d}t} = -3\gamma n \cos i & \text{(13e)} \\ \dfrac{\mathrm{d}M_0}{\mathrm{d}t} = \dfrac{3}{2}\gamma\eta n(3\cos^2 i - 1) & \text{(13f)} \end{cases}$$

where $n = \sqrt{\mu/a^3}$, $\eta = \sqrt{1-e^2}$, $\gamma = \frac{J_2 R_E^2}{2a^2\eta^4}$, and R_E is the equivalent radius of the Earth. Then,

$$\dot{\boldsymbol{f}}(\boldsymbol{x}_{\boldsymbol{\alpha}}, a_c, i_c) = \begin{pmatrix} 0 \\ \dot{M} + \dot{\omega} + \dot{\Omega}\cos i_c \\ -\dot{\omega} e \sin\omega \\ \dot{\omega} e \cos\omega \\ 0 \\ \dot{\Omega}\sin i_c \end{pmatrix} = \begin{pmatrix} 0 \\ n + \frac{3}{2}\gamma\eta n(3\cos^2 i - 1) + \frac{3}{2}\gamma n(5\cos^2 i - 1) - 3\gamma n \cos i \cos i_c \\ -\frac{3}{2}\gamma n(5\cos^2 i - 1) e \sin\omega \\ \frac{3}{2}\gamma n(5\cos^2 i - 1) e \cos\omega \\ 0 \\ -3\gamma n \cos i \sin i_c \end{pmatrix} \tag{14}$$

The expression in Eq. 12 is used to numerically propagate the state vector in the UKF.

4.3 Measurement model

The nonlinear measurement model used in this work consists of the bearing angles (azimuth, θ, and elevation, ε) that define the target heading in the platform reference frame, given by Eq. 4.

The state vector, however, is expressed in the aforementioned relative orbit element set $\delta\boldsymbol{\alpha}$. In order to obtain the expected bearing angles from a state estimate, these relative orbit elements need to be transformed into a relative position vector in the platform frame. Note that the dynamics model used considers only secular variations of the orbital elements (averaged perturbation effects). The osculating elements, which describe the instantaneous orbit that coincides with the true perturbed trajectory, are required to transform the state into actual position and velocity components.

The full transformation goes as follows:

1. The estimated mean ROE $\delta\boldsymbol{\alpha}$ and mean absolute orbital elements of the servicer $\boldsymbol{\alpha}_c$ are used to obtain the mean absolute orbital elements of the target $\boldsymbol{\alpha}_d$
2. The Brouwer-Lyddane mean-to-osculating transformation for J_2 perturbations (developed by Brouwer in [1] and modified by Lyddane in [14], available in [16] appendix F) is used to obtain the osculating absolute orbital elements of servicer and target $\widetilde{\boldsymbol{\alpha}}_c$, $\widetilde{\boldsymbol{\alpha}}_d$, from the mean absolute orbital elements $\boldsymbol{\alpha}_c$, $\boldsymbol{\alpha}_d$
3. The absolute position and velocity in inertial frame of the chief and deputy ${}^{\mathcal{N}}\boldsymbol{x}_c$, ${}^{\mathcal{N}}\boldsymbol{x}_d$, are calculated from the osculating absolute orbital elements
4. The relative position vector in the Hill frame ${}^{\mathcal{O}}\delta\boldsymbol{r}$ is calculated from the absolute Cartesian states ${}^{\mathcal{N}}\boldsymbol{x}_c$, ${}^{\mathcal{N}}\boldsymbol{x}_d$
5. The relative position vector is mapped into the platform frame using the corresponding DCMs: ${}^{\mathcal{P}}\delta\boldsymbol{r} = [PI][IO]{}^{\mathcal{O}}\delta\boldsymbol{r}$

6. The relative position vector in the platform frame is nondimensionalized and the bearing angles are calculated using Eq. 4

Although the UKF uses this full non-linear measurement model, the Brouwer-Lyddane transformation between mean and osculating elements is a first-order mapping. By performing a first-order truncation of the infinite power series solution, small errors of order J_2 are to be expected.

5. IMPLEMENTATION

5.1 Initial conditions

To test the proposed approach to use angles-only measurements obtained from a combination of trigger events in a relative orbit estimation context, three different relative orbit scenarios have been simulated. The chief mean absolute orbital elements are given in Eq. 3, while the relative orbit descriptions (in mean orbit element differences) are provided in Table 1.

The truth model is generated by propagating the initial (osculating) Cartesian state numerically with equations of motion that include Keplerian accelerations and the effect of J_2. The absolute Cartesian state of the deputy is transformed into relative position in the platform frame. The motion of the sensors is simulated to obtain the trigger events. The pointing of the corresponding sensors at the trigger events are the input for the sequential filter. A preprocessing algorithm looped at every revolution of the platform and called before the UKF time update calculates the estimated bearing angles and the time of the estimate, which serve as measurement inputs to the filtering sequence.

The initial covariance matrix is a diagonal matrix given by:

$$P_0 = \text{diag}([\sigma_a^2, \sigma_\lambda^2, \sigma_{ex}^2, \sigma_{ey}^2, \sigma_{ix}^2, \sigma_{iy}^2]) \tag{15}$$

where $\sigma_a = \sigma_{ex} = \sigma_{ey} = \sigma_{ix} = \sigma_{iy} =$ 1e-5, $\sigma_\lambda =$ 1e-3. These standard deviations are chosen to be of the same order of magnitude as the initial ROE.

The initial ROE state given to the filter is the true ROE state plus an initial state error $\boldsymbol{\epsilon}_0$:

$$\delta\boldsymbol{\alpha}_0 = \delta\boldsymbol{\alpha}_{0,\text{truth}} + \boldsymbol{\epsilon}_0 \tag{16}$$

where each component of $\boldsymbol{\epsilon}_0$ is drawn form a Gaussian distribution $\epsilon_{0,j} \sim \mathcal{N}(0, \sigma_j^2)$, with σ_j the standard deviation for each relative orbital element given above.

The servicer state is assumed perfectly known, and the measurement noise standard deviation are obtained from Table 2 for sampling frequency $f_s = 1$ Hz and angular speed $\omega = 0.5$ deg/s. No process noise models have been included at this stage.

5.2 Results

The error for each relative orbital element (solid blue) with 3-σ bounds (dotted red) are shown in Figs. 5-8. Figures 5 and 6 show the error results when the filter is given perfect measurements, while Figs. 7 and 8 show the error results using the bearing angles estimated with the approach described in Section 3. The bearing angles estimated measurements have a cadence of about 12 minutes, while the orbital periods of chief and deputy orbital periods are in the order of one thousand minutes (16 hours).

Case 1 is a relative orbit scenario in which the target has a difference in semi-major axis of 150 m and is approaching the servicer. This difference favors the observability of the problem, as it naturally acts similarly to a maneuver profile: more new information is gathered in consecutive orbits. Additionally, some short-period features of the relative orbit are range-dependent, and a variation in the range provides another metric for range estimation [17]. Case 2 is a relative orbit with only along-track separation, and the apparent motion of the target in the platform frame is an arc.

Figures 5, 6 show the error results when the filter is given perfect bearing angle measurements. For these cases, the standard deviation of the measurements is reduced by two orders of magnitude to increase the confidence on these observations. Some common trends are observed, particularly for case 1. For several

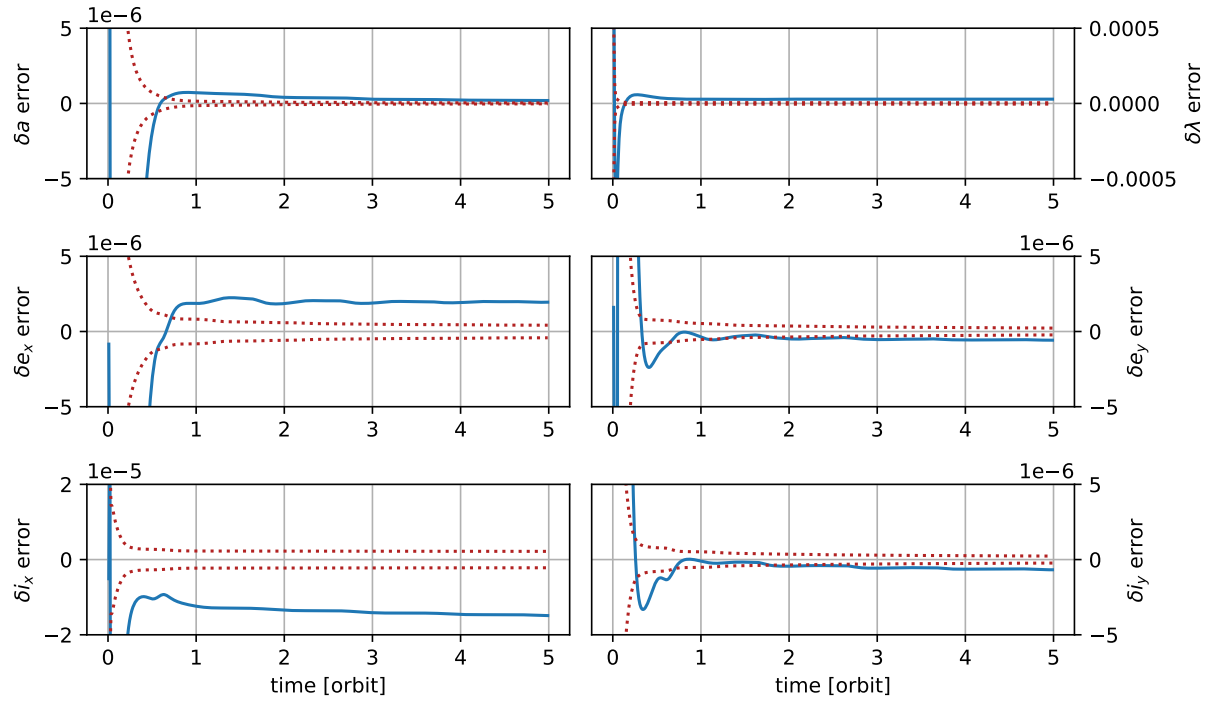

Fig. 5: Error in the estimated relative state of the target with 3-σ bounds for case 1 with perfect measurements

ROE the filter converges to a wrong value, and the error is outside the 3-σ bounds. The dynamic model propagates the mean ROE, but the measurement model uses osculating orbital elements to calculate the relative position. This mean-to-osculating transformation is performed using the Brouwer-Lyddane first order transformation, which introduces errors of up to the order of J_2

With the proposed filter configuration, the behavior of the filter becomes *smug* after about one orbit, meaning it is too confident on the current state estimate and starts rejecting measurements (state covariance becomes too small). This results in the state being propagated forward with little to no impact from new measurements.

A common approach to reduce the smugness of the filter and account for the errors being introduced by the Brouwer-Lyddane transform and any other dynamic model deficiencies, is the addition of process noise. One of the widely used methods for modeling process noise is state noise compensation, which assumes the noise in the state is additive white Gaussian noise with a known covariance. However, estimating and tuning this covariance is not trivial and this feature has not been implemented at the current stage.

Figures 7, 8 show the error results when the filter is given bearing angle measurements obtained with the process described in Section 3. By comparing Figs. 7, 8 with 5, 6, the impact of using non-perfect bearing angle estimates can be noticed. Note the difference in y-scale with respect to the previous set of figures.

The main advantage of using this relative orbital element set is that the range ambiguity is essentially confined to the relative mean longitude $\delta\lambda$. While errors or divergences are expected for this element, the remaining ROE of the set are not expected to have observability issues. However, the numerical results in this section show in some cases divergence or convergence to a different ROE value (see errors in δe_x, δi_x in Fig. 8). As seen in 3, the heading estimation results in errors with nonzero mean. This measurement bias can result in the filter converging to a wrong state. A proposed approach to handle an unknown measurement bias is augmenting the state such that the filter estimates this bias as well.

Moreover, Figs. 7, 8 show that there is a repeated structure in the errors with each orbit. This structure is related to the structure seen in the residual of the elevation angle r_ε (see Fig. 9). The measurement

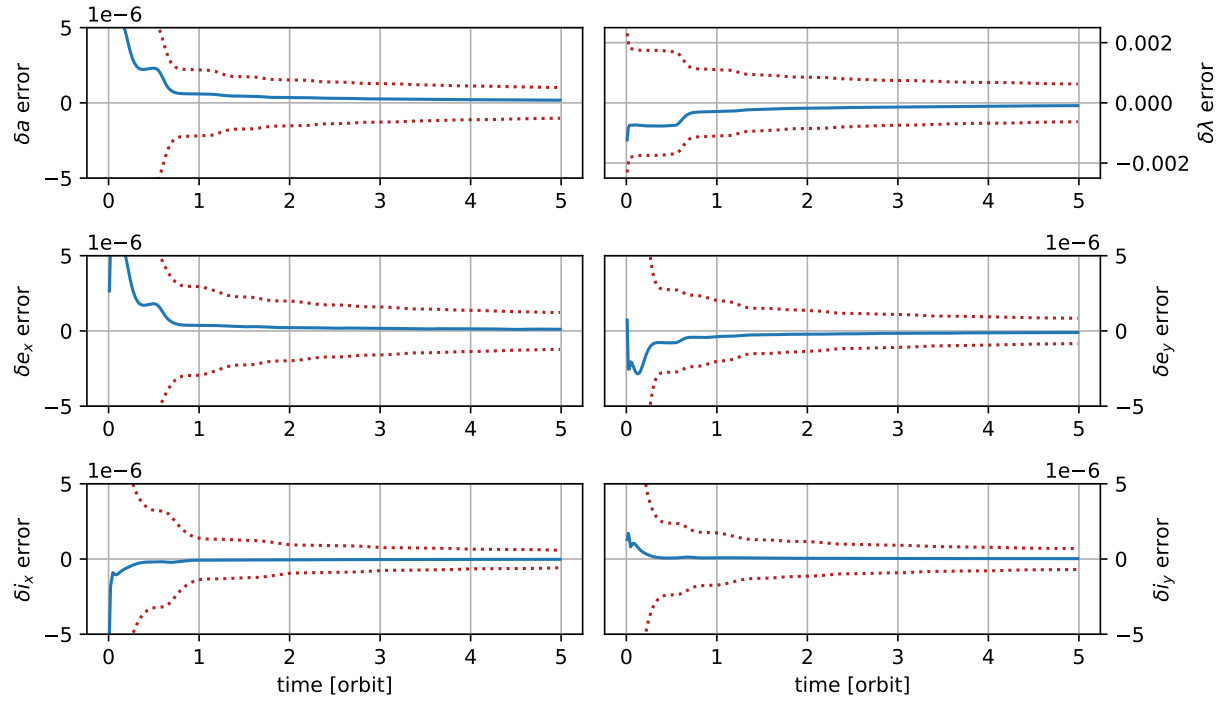

Fig. 6: Error in the estimated relative state of the target with 3-σ bounds for case 2 with perfect measurements

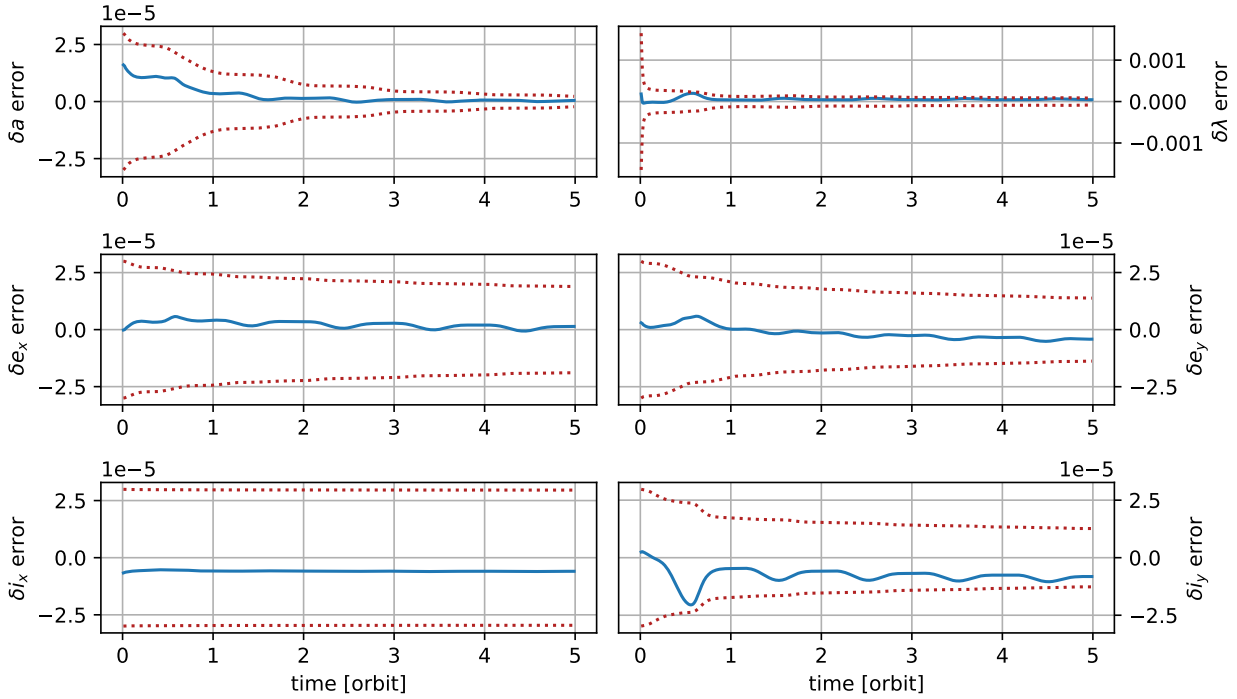

Fig. 7: Error in the estimated relative state of the target with 3-σ bounds for case 1 with estimated bearing angles

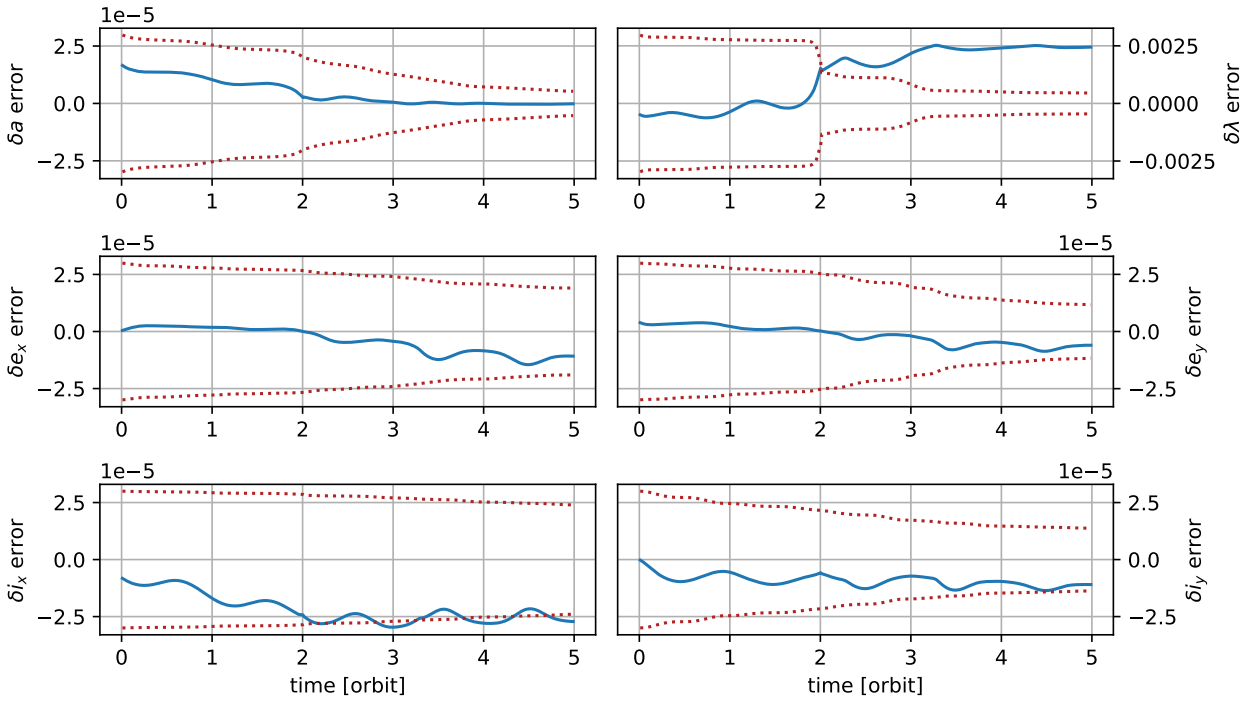

Fig. 8: Error in the estimated relative state of the target with 3-σ bounds for case 2 with estimated bearing angles

noise, and therefore the residuals, are expected to resemble white noise. Similar structures are observed in a smaller scale when using perfect measurements (see Fig. 10), hinting that the source could be related to deficiencies in the dynamics model (Brouwer-Lyddane) rather than heading estimation aspects.The possible mitigation of these structures requires further investigation.

6. CONCLUSIONS

A new method of using ambient-plasma-induced x-ray signals to estimate the relative orbit of a neighboring spacecraft was investigated. The instrument concept consists of a cluster of x-ray spectrometers with partially overlapping fields of view and mounted on a rotating platform, which records the sensor position when an acquisition or loss of signal event takes place. After a revolution of the platform is completed, these trigger events are combined to obtain an estimated heading, and the estimated bearing angles which constitute the measurement inputs to the unscented Kalman filter.

The heading estimation consists of a batch least-squares approach that assumes the target position is unchanged during the collection of trigger events. This assumption is justified because the typical time interval between trigger events ranges from seconds to tens of seconds with the parameters used, resulting in a very slight change in heading in a conventional relative orbit scenario. Factors such as angular speed of the rotation of the platform or sampling frequency have an impact in the accuracy of the estimation of the heading. The analysis performed shows that lower angular speeds and higher sampling frequencies improve the accuracy of such estimations. However, a lower angular speed of the platform implies a lower cadence of measurements, which negatively affects the performance of the filter. The parameters selected, $f_s = 1$ Hz and $\omega = 0.5$ deg/s, are a trade-off between these two effects.

Two different relative orbit cases are tested to evaluate the performance of the proposed approach in comparison with the performance with perfect measurements. Even though the errors in heading estimation obtained, of *only* a few hundredths of a degree, might seem relatively small, this translates to errors of tens

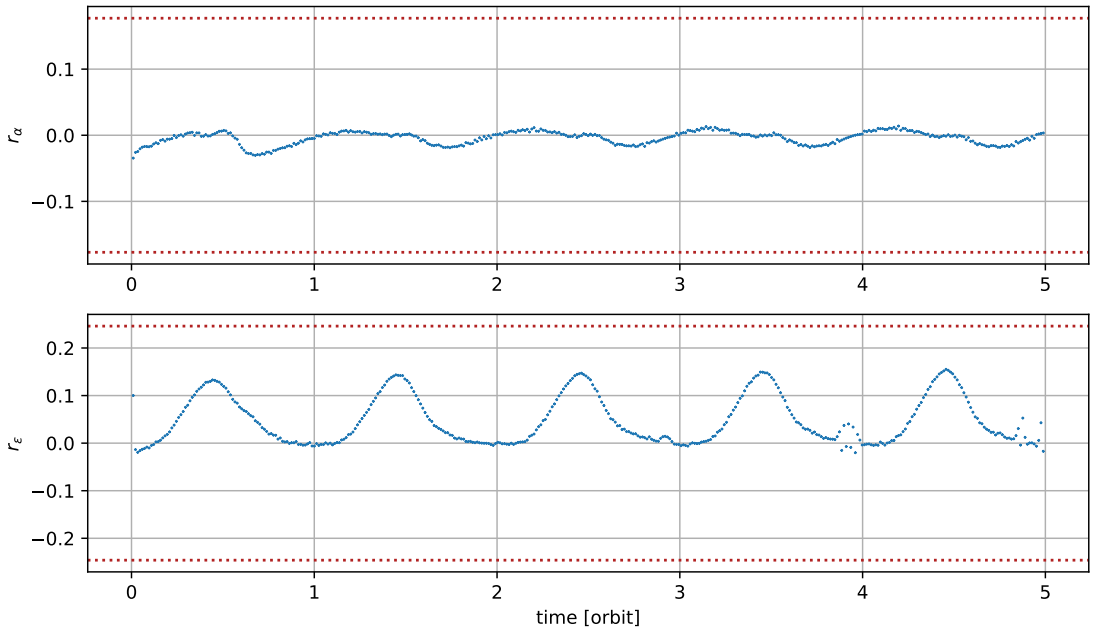

Fig. 9: Measurement residuals (blue) and 3-σ bounds (red) for case 1 with estimated bearing angles

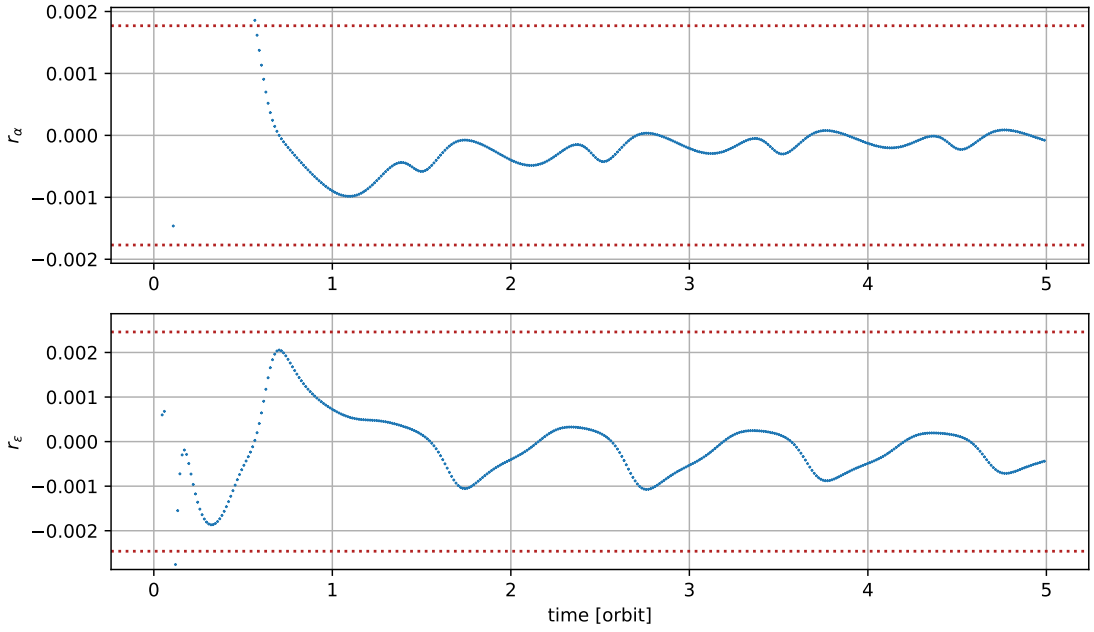

Fig. 10: Measurement residuals (blue) and 3-σ bounds (red) for case 1 with perfect measurements

of kilometers in relative position for an object that is 100 km away. In a relative orbit determination scenario, which is weakly observable, the subtle nonlinear effects can be easily hidden by errors in the measurement of the aforementioned magnitude. The use of a first order mean-to-osculating first-order transformation also plays a significant role in the accuracy of the results. A deeper analysis of the observability and the information space of the problem is required to understand the limitations of angles-only relative orbit estimation with the proposed approach.

The numerical results reveal some deficiencies in the current relative orbit determination setup. Solutions are proposed to mitigate these deficiencies, such as the inclusion of process noise to account for model deficiencies or an augmented state vector to estimate measurement biases.

REFERENCES

[1] Dirk Brouwer. Solution of the problem of artificial satellite theory without drag. *The Astronomical Journal*, 64:378, 1959.

[2] Simone D'Amico. *Autonomous formation flying in low earth orbit*. PhD thesis, TU Delft, 2010.

[3] Carolin Frueh, Kathleen Howell, K DeMars, and Surabhi Bhadauria. Cislunar Space Situational Awareness. In *31st AIAA/AAS Space Flight Mechanics Meeting*, 2021.

[4] Gabriella Gaias, Simone D'Amico, and J-S Ardaens. Angles-only navigation to a noncooperative satellite using relative orbital elements. *Journal of Guidance, Control, and Dynamics*, 37(2):439–451, 2014.

[5] Avril Haines. Annual threat assessment of the us intelligence community. *Office of the Director of National Intelligence*, 9, 2021.

[6] JS Halekas, Y Saito, GT Delory, and WM Farrell. New views of the lunar plasma environment. *Planetary and Space Science*, 59(14):1681–1694, 2011.

[7] Simon J Julier and Jeffrey K Uhlmann. New extension of the kalman filter to nonlinear systems. In *Signal processing, sensor fusion, and target recognition VI*, volume 3068, pages 182–193. Spie, 1997.

[8] Spencer Kaplan. Eyes on the Prize. The Strategic Implications of Cislunar Space and the Moon, 2020.

[9] Evan Kaufman, T Alan Lovell, and Taeyoung Lee. Nonlinear observability for relative orbit determination with angles-only measurements. *The Journal of the Astronautical Sciences*, 63:60–80, 2016.

[10] Bhavya Lal, Asha Balakrishnan, Becaja M Caldwell, Reina S Buenconsejo, and Sara A Carioscia. Global trends in Space Situational Awareness (SSA) and Space Traffic Management (STM). Technical report, Institute for Defense Analyses, 2018.

[11] Andrea López, Julian Hammerl, and Hanspeter Schaub. Detecting space objects with binary wide field of view x-ray sensing. In *AAS Astrodynamics Specialist Conference*, Charlotte, NC, Aug. 7–10 2022. Paper No. AAS 22-602.

[12] Andrea López, Julian Hammerl, and Hanspeter Schaub. Dynamic detection of nearby space objects with binary wide field of view x-ray sensing. In *AIAA SciTech*, National Harbor, Maryland, January 23–28 2023.

[13] T Alan Lovell and Taeyoung Lee. Nonlinear observability for relative satellite orbits with angles-only measurements. In *24 th International Symposium on Space Flight Dynamics*, 2014.

[14] RH Lyddane. Small eccentricities or inclinations in the brouwer theory of the artificial satellite. *Astronomical Journal, Vol. 68, p. 555 (1963)*, 68:555, 1963.

[15] Barry C Roberts. Cross-Program Design Specification for Natural Environments (DSNE) Revision I. Technical report, NASA, 2021.

[16] Hanspeter Schaub and John L Junkins. *Analytical mechanics of space systems*. Aiaa, 2003.

[17] Joshua Sullivan and Simone D'Amico. Nonlinear kalman filtering for improved angles-only navigation using relative orbital elements. *Journal of Guidance, Control, and Dynamics*, 40(9):2183–2200, 2017.

[18] Eric A Wan and Rudolph Van Der Merwe. The unscented kalman filter for nonlinear estimation. In *Proceedings of the IEEE 2000 Adaptive Systems for Signal Processing, Communications, and Control Symposium (Cat. No. 00EX373)*, pages 153–158. Ieee, 2000.

[19] Kieran TH Wilson, Julian Hammerl, and Hanspeter Schaub. Using plasma-induced x-ray emission to estimate electrostatic potentials on nearby space objects. *Journal of Spacecraft and Rockets*, 59(4):1402–1405, July–Aug. 2022.

[20] David C Woffinden and David K Geller. Observability criteria for angles-only navigation. *IEEE Trans-*

actions on Aerospace and Electronic Systems, 45(3):1194–1208, 2009.

A. UNSCENTED KALMAN FILTER

The core difference between the unscented Kalman filter (UKF) and other filters such as the extended Kalman filter (EKF) is the manner in which Gaussian random variables (GRV) are represented for their propagation. The EKF approximates the state distribution as a GRV, and the propagation of the covariance is done using a first-order linearization of the nonlinear system, which can lead to inaccuracies and divergence of the filter, especially when the system is highly nonlinear. In contrast, the UKF uses a deterministic sampling approach: the state distribution is still approximated by a GRV, but a set of sample points (called *sigma* points) are used to represent this GRV, capturing its mean and covariance. When propagating these sample points with the nonlinear equations of motion, the posterior mean and covariance of the GRV are accurately represented to second order [18].

The UKF is based on the Unscented Transform (UT), which is a method for calculating the statistics of a GRV that undergoes a nonlinear transformation through a set of sigma points. For a variable $\boldsymbol{x}_k$ with mean $\bar{\boldsymbol{x}}_k$ and covariance $P_{\boldsymbol{x},k}$ at time k, the sigma points are given by:

$$\begin{aligned}
\mathcal{X}_{\prime,\|} &= \bar{\boldsymbol{x}}_k, \\
\mathcal{X}_{i,k} &= \bar{\boldsymbol{x}}_k + (\sqrt{(L+\gamma)P_{\boldsymbol{x},k}})_i, && i = 1, ..., L, \\
\mathcal{X}_{i,k} &= \bar{\boldsymbol{x}}_k - (\sqrt{(L+\gamma)P_{\boldsymbol{x},k}})_{i-L}, && i = L+1, ..., 2L
\end{aligned} \tag{A1}$$

where $\lambda = \alpha^2(L+\kappa) - L$ is a scaling parameter. The constant α determines the spread of the sigma points around the mean and is typically set to a small positive value, κ is a secondary scaling parameter typically set to 0 or $3 - L$, and L is the dimension of the state $\boldsymbol{x}$. These sigma vectors are propagated with the corresponding nonlinear function $\mathcal{X}_{i,k+1} = f(\mathcal{X}_{i,k})$. The mean and covariance at the next time step are

$$\bar{\boldsymbol{x}}_{k+1} \approx \sum_{i=0}^{2L} W_i^{(}m)\mathcal{X}_{i,k+1} \tag{A2}$$

$$P_{\boldsymbol{x},k+1} \approx \sum_{i=0}^{2L} W_i^{(}c)(\mathcal{X}_{i,k+1} - \bar{\boldsymbol{x}}_{k+1})(\mathcal{X}_{i,k+1} - \bar{\boldsymbol{x}}_{k+1})^T \tag{A3}$$

with W_i weights given by

$$\begin{aligned}
W_0^{(}m) &= \frac{\lambda}{L+\lambda}, \\
W_0^{(}c) &= \frac{\lambda}{L+\lambda} + 1 - \alpha^2 + \beta, \\
W_i^{(}m) &= W_i^{(}c) = \frac{1}{2(L+\lambda)}, && i = 1, ..., 2L
\end{aligned} \tag{A4}$$

where the constant β is used to incorporate prior knowledge of the distribution $\boldsymbol{x}$ and is set to $\beta = 2$ for Gaussian distributions.

The generic equations for the UKF are given in Table A1.

Table A1: Unscented Kalman filter (UKF) equations [18]

Initialize with:

$$\hat{\boldsymbol{x}}_0 = \mathbb{E}[\boldsymbol{x}_0] \tag{A5}$$

$$P_0 - \mathbb{E}[(\boldsymbol{x}_0 - \hat{\boldsymbol{x}}_0)(\boldsymbol{x}_0 - \hat{\boldsymbol{x}}_0)^T] \tag{A6}$$

For $k \in \{1, ..., \infty\}$,
Calculate sigma points:

$$\mathcal{X}_{k-1} = \begin{bmatrix} \hat{\boldsymbol{x}}_{k-1} & \hat{\boldsymbol{x}}_{k-1} + \gamma\sqrt{P_{k-1}} & \hat{\boldsymbol{x}}_{k-1} - \gamma\sqrt{P_{k-1}} \end{bmatrix} \tag{A7}$$

Time update:

$$\mathcal{X}_{k|k-1} = \boldsymbol{F}[\mathcal{X}_{k-1}] \tag{A8}$$

$$\hat{\boldsymbol{x}}_k^- = \sum_{i=0}^{2L} W_i^{(m)} \mathcal{X}_{i,k|k-1} \tag{A9}$$

$$P_k^- = \sum_{i=0}^{2L} W_i^{(c)} [\mathcal{X}_{i,k|k-1} - \hat{\boldsymbol{x}}_k^-][\mathcal{X}_{i,k|k-1} - \hat{\boldsymbol{x}}_k^-]^T + Q \tag{A10}$$

$$\mathcal{Y}_{k|k-1} = \boldsymbol{H}[\mathcal{X}_{k|k-1}] \tag{A11}$$

$$\hat{\boldsymbol{y}}_k^- = \sum_{i=0}^{2L} W_i^{(m)} \mathcal{Y}_{i,k|k-1} \tag{A12}$$

Measurement update equation:

$$P_{\boldsymbol{y}_k,\boldsymbol{y}_k} = \sum_{i=0}^{2L} W_i^{(c)} [\mathcal{Y}_{i,k|k-1} - \hat{\boldsymbol{y}}_k^-][\mathcal{Y}_{i,k|k-1} - \hat{\boldsymbol{y}}_k^-]^T + R \tag{A13}$$

$$P_{\boldsymbol{x}_k,\boldsymbol{y}_k} = \sum_{i=0}^{2L} W_i^{(c)} [\mathcal{X}_{i,k|k-1} - \hat{\boldsymbol{x}}_k^-][\mathcal{Y}_{i,k|k-1} - \hat{\boldsymbol{y}}_k^-]^T \tag{A14}$$

$$K_k = P_{\boldsymbol{x}_k,\boldsymbol{y}_k} P_{\boldsymbol{y}_k,\boldsymbol{y}_k}^{-1} \tag{A15}$$

$$\hat{\boldsymbol{x}}_k = \hat{\boldsymbol{x}}^- + K_k(\boldsymbol{y}_k - \hat{\boldsymbol{y}}_k^-) \tag{A16}$$

$$P_k = P_k^- = K_k P_{\boldsymbol{y}_k,\boldsymbol{y}_k} K_k^T \tag{A17}$$

where $\gamma = \sqrt{(L + \lambda)}$, λ=composite scaling parameter, L=dimension of the state, Q=process noise covariance, R=measurement noise covariance, W_i=weights as calculated in Eq. A4.